8-1-2006

Fatigue Crack Growth Mechanisms At the Microstructure Scale in Al-Si-Mg Cast Alloys: Mechanisms in Regions II and III

Diana A. Lados
Worcester Polytechnic Institute, lados@wpi.edu

Diran Apelian
Worcester Polytechnic Institute, dapelian@wpi.edu

J. Fred Major

Fatigue Crack Growth Mechanisms at the Microstructure Scale in Al-Si-Mg Cast Alloys: Mechanisms in Regions II and III

DIANA A. LADOS, DIRAN APELIAN, and J. FRED MAJOR

The fatigue crack growth behavior in Regions II and III of crack growth was investigated for hypoeutectic and eutectic Al-Si-Mg cast alloys. To isolate and establish the mechanistic contributions of characteristic microstructural features (dendritic α-Al matrix, eutectic phases, Mg-Si strengthening precipitates), alloys with various Si content/morphology, grain size level, and matrix strength were studied; the effect of secondary dendrite arm spacing (SDAS) was also assessed. In Regions II and III of crack growth, the observed changes in the fracture surface appearance were associated with changes in crack growth mechanisms at the microstructural scale (from a linear advance predominantly through primary α-Al to a tortuous advance exclusively through Al-Si eutectic Regions). The extent of the plastic zone ahead of the crack tip was successfully used to explain the changes in growth mechanisms. The fatigue crack growth tests were conducted on compact tension specimens under constant stress ratio, $R = 0.1$, in ambient conditions.

I. INTRODUCTION AND BACKGROUND

CASTING defects such as shrinkage and gas porosity, oxides, and other types of inclusions dominate fatigue behavior; the more and larger the defects the lower the fatigue performance. Interdendritic shrinkage pores;[1–5] gas pores of different amount, size, and distribution;[4–11] old and new oxide films; and other inclusions[2,3,8] act as crack initiators and facilitate crack growth reducing the overall performance of the cast component. There is a hierarchy among the factors that control fatigue behavior,[12] and when one dominating factor (defect) is reduced under certain levels, the next one becomes operative.

As defect levels are decreased through advanced molten metal processing methods, the intrinsic microstructural features of the alloy begin to dictate the fatigue behavior of the component. Thus, fatigue crack initiation from pre-existing casting defects is replaced by initiation from either persistent slip bands in the dendrite cells[2,5] or at the eutectic Si particles.[9,10,11] Predictive models based on the amount, size, and morphology of casting defects become less germane, and an understanding of both initiation and propagation mechanisms from a microstructural point of view becomes imperative. Specifically, small-scale microstructural features, such as secondary dendrite arm spacing (SDAS) (*i.e.*, size and strength of the α-Al matrix)[13–18] and Si particles (*i.e.*, morphology, distribution, and Si particle/matrix interface strength)[17,19,20] play a critical role in the fatigue and fatigue crack growth behavior of cast Al-Si alloys. However, a mechanistic knowledge based on the effects of these scalar features on fatigue and fatigue crack growth is still lacking, mainly because of the difficulties entailed in separating the effects of these variables.

DIANA A. LADOS, Research Assistant Professor, and DIRAN APELIAN, Professor, are with the Worcester Polytechnic Institute, Metal Processing Institute, Worcester, MA 01609. Contact e-mail: lados@wpi.edu J. FRED MAJOR, Research Scientist, is with Alcan International Ltd., Kingston, ON K7L 5T4, Canada.

Manuscript submitted November 22, 2005.

The relationships between microstructure and initial stages of crack formation and slow propagation, ΔK_{th} and Region I, for both long and small cracks have been studied by Lados *et al.*[21] In brief, the long crack threshold behavior of the materials was attributed to combined effects of microstructure/roughness induced and residual stress (introduced during heat treatment) induced closure mechanisms. On the other hand, the near-threshold response of small cracks was explained through nonclosure related mechanisms when the barrier effects of characteristic microstructural features dictate the alloy's behavior.

This work focuses on the growth mechanisms of long cracks in Regions II and III. The observed changes in crack growth mechanisms at the microstructural scale are explained through an increase in the extent of the damaged zone ahead of the crack tip (plastic zone) with increasing crack driving force and crack length. The extent of the plastic zone together with the type/amount/morphology of damaged microstructural features enclosed in the plastic zone are used to explain the crack's path selection at different stages of fatigue crack growth.

II. EXPERIMENTAL PROCEDURE

Al-Si-Mg alloys of fixed Mg content (0.45 pct) and three Si levels, 1, 7, and 13 pct, were investigated.* The Si levels were selected such that each microstructural constituent specific to this class of alloys was individually represented, *i.e.*, the primary α-Al dendritic structure in the 1 pct Si alloy; the Al/Si eutectic structure in the 13 pct Si alloys; and a hypoeutectic, hybrid structure in which the two phases coexist in the 7 pct Si alloys (alloys resembling the microstructure of commercial A356/357 alloys). High-purity alloys were used, with all other elements kept at low levels ($<$0.002 pct). The Fe, the major impurity in commercial cast alloys, was kept at a concentration below 0.02 pct. The eutectic Si in the 7 and 13 pct Si alloys was

*All compositions are given in weight percent.

studied in both unmodified (UM; UM is used from here forward to represent the Unmodified eutectic Si structure) and Sr-modified (M; M is used from here forward to represent the Sr-modified eutectic Si structure) conditions. The eutectic Si was modified using a commercial Al-10 pct Sr master alloy, and appropriate additions for each Si content were made: 0.018 to 0.021 pct Sr for the 7 pct Si alloys and 0.024 to 0.027 pct Sr for the 13 pct Si alloys. The average size and shape factors of the Si particles for each condition, as observed after heat treatment, are given in Table I. The distance between consecutive eutectic Si particles was found to be ~2 to 10 μm depending on the degree of modification; the distance between interdendritic eutectic Regions was found to be ~20 to 30 μm, similar to the SDAS of the material. The mean free path between three-grain junction eutectic zones was in the 75- to 200-μm range.

A secondary dendrite arm spacing of 20 to 30 μm was attained in all the prepared alloys by controlling the freezing rate in a specifically designed sand mold containing top and bottom chills. All alloys were grain refined using additions of a commercial Al-5 pct Ti-1 pct B master alloy. To achieve the same grain size irrespective of alloy, the amount of grain refiner was adjusted depending on the Si level of the alloy and the extent of the eutectic Si modification. Three grain size levels were studied; grain refiner levels for each alloy and condition are given in Table II. The majority of the studies were conducted on samples with a grain size in the 280- to 320-μm range.

A modified T61 heat treatment using an uphill/reverse quench was applied to all samples. The uphill/reverse quench was used to produce residual stress-free samples and to eliminate residual stress effects from the analysis. The heat treatment consisted of solution treatment for 1.5 hours at 538 °C, boiling water quench for 15 minutes, liquid N_2 immersion for 30 minutes, boiling water reverse quench for 15 minutes, natural aging for 12 hours at room temperature; and artificial aging for 12 hours at 155 °C. Sample transfer time from one medium to another was less than 2 seconds.

Table I. Average Si Particle Size and Shape Factor for the UM and M 7 Pct Si and 13 Pct Si Alloys

	Alloy Systems Examined			
	7 Pct Si-UM	7 Pct Si-M	13 Pct Si-UM	13 Pct Si-M
Si average particle size (μm)	2.77	2.19	2.94	2.05
Si particle shape factor*	1.41	1.21	1.86	1.19

*Shape factor was calculated as shape factor = perimeter^2/(4 · π · area).

In all alloys prepared and studied, both the primary α-Al and the α phase of the eutectic had similar microhardness values of 100 to 105 HV. The effect of matrix strength on fatigue crack growth was investigated by introducing an additional condition of increased ductility in the 7 pct Si alloys by applying a T4 heat treatment consisting of solutionizing, uphill/reverse quench, and natural aging. The absence of artificial aging prevented the development of Mg-Si strengthening precipitates, and the matrix microhardness decreased to 80 to 85 HV. Samples with lower yield strength and higher ductility compared to the T61 samples were thus obtained (Table III).

The microstructures of all five alloys after heat treatment are presented in Figures 1(a) through (e). The level of porosity was kept very low (<0.005 pct) in all the alloys studied so that pores would not significantly interfere with the advancement of the crack.

For the fatigue crack growth studies, compact tension specimens with nominal dimensions of 95 mm × 91 mm × 10 mm were machined from the heat-treated castings. The notch length was 38 mm measured from the front face of the sample and 19 mm measured from the pin holes. The notch opening was 0.15 mm. Tests were conducted according to ASTM E647 in laboratory air at room temperature, 24 °C, and relative humidity 40 to 50 pct. The specimens were tested under K control (first decreasing, Region I, and then increasing, Regions II and III). Above 10^{-3} mm/cycle, the test was continued using a shallower K-gradient to obtain the steeper Region III data. The upper limit of the crack driving force was referred to as the ''pseudo'' fracture toughness of the materials, because the crack growth specimens did not meet the dimensional requirements for plane strain fracture toughness. The compliance technique was used to monitor the crack advance and the frequency was set to 25 Hz, except in Region III, where it was decreased to capture sufficient data points. All samples were tested at constant stress ratio, $R = 0.1$.

To prepare samples for fractographic analysis, half of the compact tension specimens were vertically sectioned through the middle of the thickness and mounted in such a way that the side view of the crack was revealed for optical microscopy and SEM examination, while the other half was used for top view observations and roughness measurements of the fracture surfaces.

For roughness measurements, a three-dimensional (3-D) WYKO RST-Plus noncontact profilometer was used applying white light interferometry in vertical scanning mode to

Table II. Titanium Levels (in Weight Percent) Corresponding to Three Grain Sizes for All Alloys in UM and M Conditions

Grain Size (μm)	Alloy Systems Examined				
	1 Pct Si	7 Pct Si-UM	13 Pct Si-UM	7 Pct Si-M	13 Pct Si-M
180 to 220	0.0080 to 0.0090	0.080 to 0.090	—†	0.070 to 0.080	0.27 to 0.33
280 to 320	0.0065 to 0.0075	0.035 to 0.045	0.25 to 0.30	0.025 to 0.035	0.20 to 0.25
~520	—	0.0007 to 0.0009	—	0.0004 to 0.0006	—

†— = Case not included in the study.

measure surface topography. The as-measured 3-D profiles were characterized by a waviness component and a roughness component. To remove the waviness component from the profile, the Mountains Map software was used, and Gaussian filters, defined by judiciously selected (alloy dependent) cutoff lengths, were applied. The waves longer than the cutoff length were classed as waviness, while the waves shorter than the cutoff length were considered roughness. The roughness component represents essentially the microstructure related fracture surface variations with respect to a standard horizontal line; an appropriate roughness parameter was selected and used in the analysis (Section III–A).

Table III. Ultimate Tensile Strength (UTS), Yield Strength (YS), and Elongation (Pct) for UM and M Alloys in T61 and T4 Heat-Treating Conditions (Tested at Room Temperature per ASTM B557)

	UTS		YS		
Alloy	US (ksi)	SI (MPa)	US (ksi)	SI (MPA)	Total Elongation (Pct)
1 Pct Si-T61	40.6	280.2	29.6	204.2	13.93
7 Pct Si-UM-T61	45.1	311.3	33.9	233.7	7.34
7 Pct Si-M-T61	45.2	312.0	35.0	241.0	6.08
7 Pct Si-UM-T4	38.5	265.8	20.1	138.7	11.95
7 Pct Si-M-T4	38.3	264.5	20.2	139.4	14.69
13 Pct Si-UM-T61	51.5	355.0	38.3	264.1	7.47
13 Pct Si-M-T61	49.7	342.7	39.0	269.1	7.33

III. RESULTS AND DISCUSSION

In the following sections, the mechanisms active at different stages during the stable crack propagation (Region II) and fast fracture mode (Region III) are discussed with emphasis on their relationship with the microstructure.

A. *Crack Propagation Mechanisms in Paris Region II and Region III for 7 Pct Si and 13 Pct Si Alloys*

The long fatigue crack growth behavior from threshold to pseudo-fracture toughness for both UM and M alloys is presented in Figures 2(a) and (b).

It has been shown that closure mechanisms govern the crack growth behavior of the alloys in the near-threshold regime (Region I), where the small crack tip opening displacements allow considerable interference between the crack surface asperities, facilitating the occurrence of closure.[21] However, with increasing crack driving force and crack tip opening displacements, the shielding of the crack tip due to closure mechanisms diminishes as the surface interference becomes progressively a smaller amount of the total crack-tip opening displacement. Therefore, even though the closure level remains almost constant (Figure 3), its influence on the crack growth rate considerably diminishes as the cyclic stress intensity increases from the upper near-threshold regime to Paris Region II. In Figure 3, the crack closure lever, K_{cl}, was calculated as $K_{cl} = K_{max} - \Delta K_{eff}$, where ΔK_{eff} was evaluated using the adjusted compliance ratio technique.[22]

Once closure mechanisms become less important, fatigue crack growth mechanisms become strongly dependent on

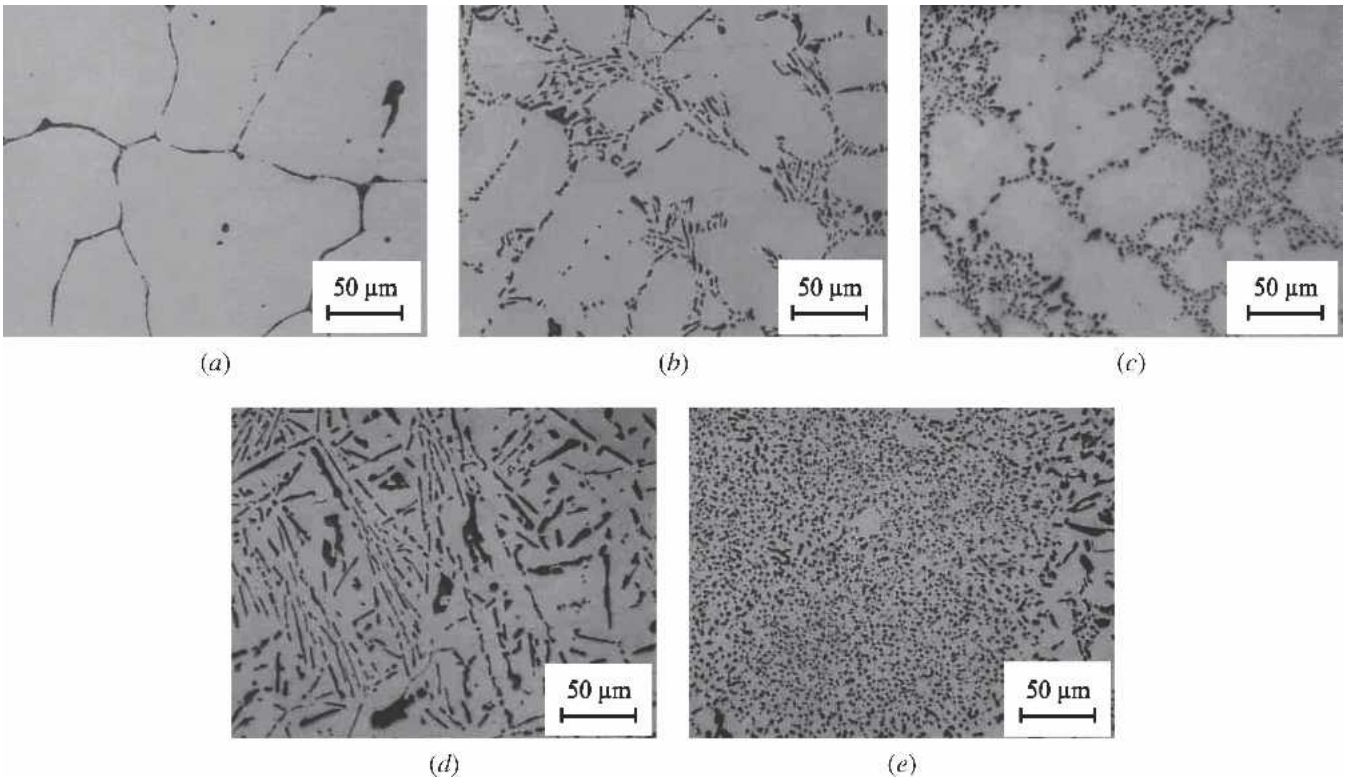

Fig. 1—Alloy microstructures after heat treatment (etched with 1 pct HF for 10–15 seconds): (*a*) 1 pct Si; (*b*) 7 pct Si-UM; (*c*) 7 pct Si-M; (*d*) 13 pct Si-UM; (*e*) 13 pct Si-M.

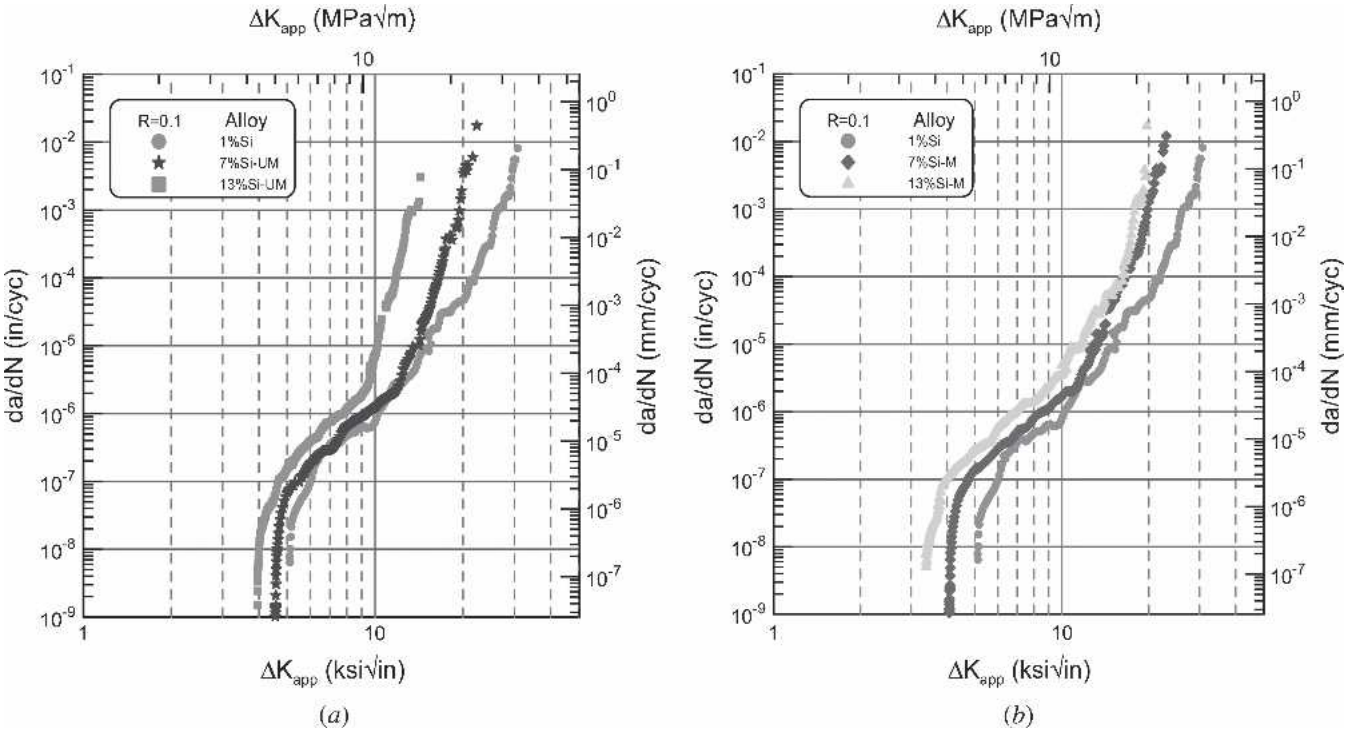

Fig. 2—Fatigue crack growth behavior of the alloys studied: (*a*) UM family, and (*b*) M family.

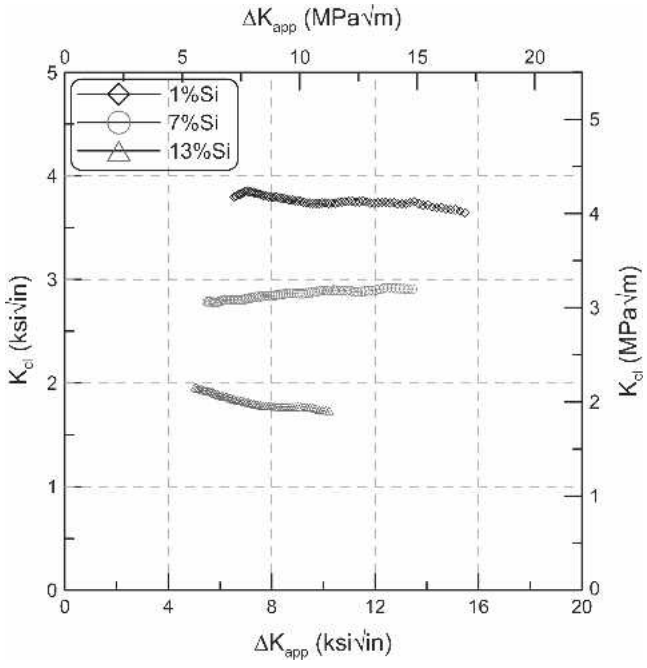

Fig. 3—Evolution of closure levels with increasing ΔK for 1 pct Si, 7 pct Si, and 13 pct Si alloys.

the α-Al matrix strength, the bonding strength at the interface between the α-Al structure and eutectic Si particles, and the strength of the Si particles. As a general rule, a crack always seeks the path of least resistance offered by the most damaged microstructural features ahead of it. This rule leads to the understanding of the operative mechanisms causing the microstructural changes observed at different stages during crack growth.

The fracture surfaces of all tested samples revealed a significant increase in roughness, from a rather flat crack path (mainly perpendicular to the loading axis) to a highly tortuous one, as the crack propagated from lower Region II to lower Region III. The changes in surface roughness, captured for each alloy in lower Region II and lower Region III, are presented in Figures 4(a) and (b).

The surface roughness index (SRI), defined as the true fracture surface length divided by the length of a straight line drawn between the same end points, can be used to quantify fracture surface roughness. An example of the increase in roughness between different stages of crack growth is shown in Figures 5(a) and (b) for a M 7 pct Si alloy. The SRI increased from 1.2 in lower Region II to 1.8 in lower Region III. This increase in roughness was accompanied by an increase in crack growth rate from 0.0066 to 0.093 μm/cycle.

For the 7 pct Si alloys, the observed changes in roughness are associated with a gradual change in propagation mechanisms at the microstructure scale. At low ΔK levels, the flat fracture surface corresponds to an advance of the crack through the primary α-Al matrix or, more appropriately, through the microstructural constituent found directly ahead of the crack (which is mainly the α-Al structure) with occasional encounters with Si particles favorably located straight ahead of the crack tip. This can be explained by considering that the surface area percentage covered by the α-Al matrix phase is predominant (~85 pct), the rest being populated with eutectic Si. With increasing ΔK, fracture surfaces reveal an increasing number of Si particles indicating an increasing crack preference for interaction with Si particles. At high ΔK, the crack preferentially progresses through Al-Si eutectic Regions and its appearance becomes increasingly tortuous. A crack's general

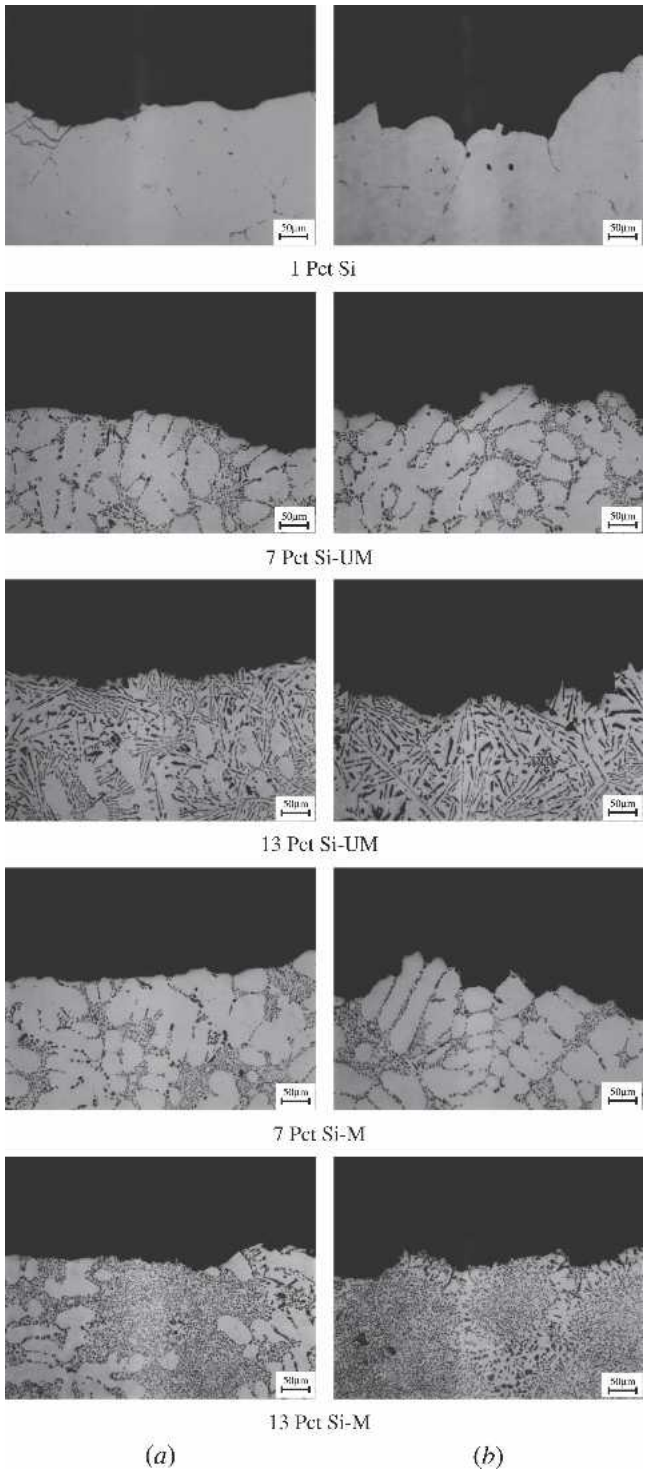

Fig. 4—Changes in fracture surface roughness of the studied alloys with increasing ΔK: (*a*) lower Region II (left column), and (*b*) lower Region III (right column).

tendency is to grow perpendicular to the direction of load application unless damaged material away from the crack front makes it energetically more favorable to abandon the straight advance and to start meandering. An increasing number of Si particles along the crack path with increasing stress intensity factor range and crack length has been previously reported.[19,23,24] These changes in mechanisms can be explained by considering the amount of damaged material ahead of the crack tip at various stress intensity levels. The monotonic plastic zone size was found to be the appropriate parameter to characterize the extent of the damaged material and to correlate ΔK levels with fatigue crack growth mechanisms that occur at the microstructure level.

The use of the monotonic plastic zone instead of the cyclic plastic zone was based on two considerations. First, it reflects more accurately the stress intensity levels at which changes in crack growth mechanisms occur, as revealed by the fractographic observations. Second, the damage to the Al-Si interfaces or Si particles is the rate controlling parameter in crack propagation, and this tensile damage is mainly introduced on maximum loading of each cycle ($K_{\max}$ process). The remaining part of the cycle causes compressive damage mostly to the α-Al matrix inside the cyclic plastic zone. Additionally, from a fracture mechanics point of view, a factor of four difference between monotonic and cyclic plastic zones applies only for a stress ratio $R = 0$; for higher stress ratios, the difference can become as large as 40, which will lead to unrealistically small cyclic plastic zones. An expression for the monotonic plastic zone, Eq. [1], that takes into account both effects from plane stain and plane stress was developed,[25] and this equation has been used to compute the extent of the damaged material ahead of the crack tip at different stress intensity levels. Note that for simplicity, the same cardioid shape was assumed for the entire range from plane strain to plane stress, the only difference consisting in plastic zone size.

$$r_p \approx \left(\frac{1}{2\pi}\right)^n \left(\frac{1}{6\pi}\right)^{1-n} \frac{K_{\max}^2}{\sigma_{YS}^2} \cos^2\frac{\theta}{2}\left(1 + 3\sin^2\frac{\theta}{2}\right) \qquad [1]$$

where n = degree of plane stress = $0 < n \leq 1$; and B = specimen thickness. $= \dfrac{1.33 \cdot r_{p(\text{plane-stress})}}{B}$

Plastic strain is the most damaging parameter in fatigue and therefore the size of the plastic zone at the crack tip is decisive for the future advance of the crack. The damaged microconstituents enclosed in the plastic zone are preferred by the crack. Thus, a relationship between the plastic zone size and the dimensions of the microconstituents specific to the alloys is critical for understanding the fatigue crack growth behavior at different stages.

The plastic zone radius computed using Eq. [1] needs to be compared with the critical microstructural feature that controls the crack advance. In the case of alloys with significant eutectic content, such as 7 pct Si alloys, this critical feature is the SDAS. For the alloys studied, the average SDAS was ~25 μm, implying that a plastic zone at least that large will contain Si particles that have been either damaged or whose interfaces with the α-Al matrix have been weakened and can provide a weak link for the incoming crack. A plastic zone, $r_p \sim$ SDAS, corresponds to a crack driving force, $\Delta K \approx 5.5$ MPa$\sqrt{\text{m}}$ (5 ksi$\sqrt{\text{in.}}$), which on the fatigue crack growth curves corresponds roughly to the transition point from near-threshold regime to stable growth in Paris Region II. The deflective role (determining the level of closure) attributed to the Si particles in the near-threshold regime[21] becomes a crack advancing decohesion

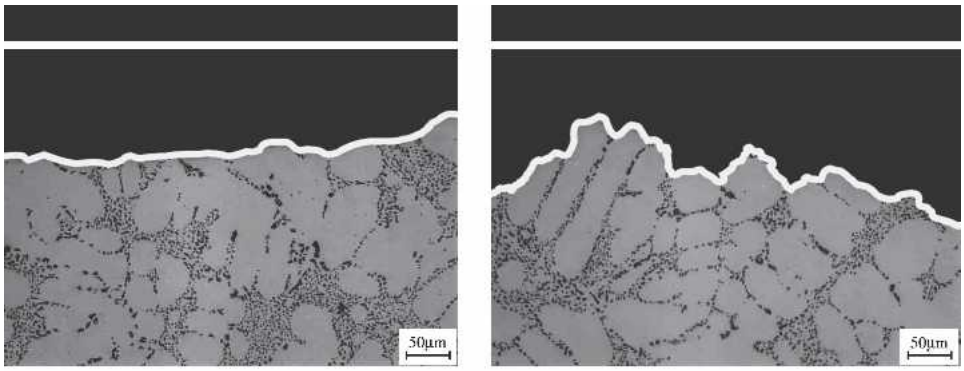

Fig. 5—Changes in fracture surface roughness with increasing crack driving force for a M 7 pct Si alloy: (*a*) lower Region II ($\Delta K \sim 5.5$ MPa$\sqrt{\text{m}}$), and (*b*) lower Region III ($\Delta K \sim 12$ MPa$\sqrt{\text{m}}$).

mechanism that represents the most probable failure mode at low crack driving forces.[19,24] Small plastic zones, when the Si particle size is significant at the scale of the plastic zone size, cannot provide the strain energy required to fracture Si particles unless the particles have high aspect ratio and their principal axis is perpendicular to the crack plane. In such cases, Si particles have a high resistance to debonding due to the large interface area located parallel to the loading direction,[26] and thus they are more likely to fracture. It was observed that high aspect ratio Si particles with an inclination angle to the crack plane lower than 45 deg or higher than 135 deg have a tendency to debond (Figures 6(a) and (d)), while particles with angles between 45 and 135 deg are expected to break, even at low crack driving forces (Figures 6(b) and (d)). However, when a Si twin plane is parallel to the crack front, Si particles can fracture at angles lower than 45 deg or higher than 135 deg, Figure 6(c).

The decohesion/fracture mechanism is a result of plastic deformation ahead of the crack tip, which involves dislocation pileups along the slip planes when an obstacle such as a Si particle is encountered. The high shear stress buildup at the head of dislocation pileups can nucleate a microcrack, and, depending on the stored elastic strain energy, the microcrack can either stagnate, crack the Al-Si interface bonds (decohesion), or provide the stress concentration necessary to weaken and fracture the Si particles. The damage mechanisms are cumulative processes where the mixed effects of stress intensity level and Si particle morphology, orientation, and distribution dictate the dominant damage mechanism.

At low crack driving forces, even though the plastic zone starts sampling Si particles, the amount of Si particles on the fracture surface is low, and the appearance of the crack is flat and dominated by the presence of primary α-Al matrix. The crack's opportunity to ''select'' weak Si particles is restricted to sporadic particles found in the immediate vicinity of the crack and almost in line with the crack tip. Thus, the crack advances through the damaged dendritic structure, and when Si particles with weakened interfaces are encountered, the crack follows the weaker path provided by the Si; however, the availability of Si particles is rather limited at ΔK values between 5 and 9 MPa$\sqrt{\text{m}}$ (4.5 and 8 ksi$\sqrt{\text{in.}}$), Figure 7(a) (left).

As ΔK increases, the number of Si particles on the surface increases as well, and the crack's bias toward advancement around/along or through Si particles becomes more and more evident. For the crack to exclusively follow Si particles, it is necessary to constantly locate ahead of it Si particles that have undergone prior damage (either debonding or cracking). This requirement implies a plastic zone size that samples a significant number of Si particles and provides a continuous path of increasingly weaker Si links. In this case, it becomes energetically more favorable for the crack to deviate from the planar advancement and meander through the Regions of least resistance. For the case of 7 pct Si alloys, in lower Region II, the crack interacts with individual particles, then, at $\Delta K > 8$ to 9 MPa$\sqrt{\text{m}}$ (7 to 8 ksi$\sqrt{\text{in.}}$), Figure 7(a) (middle), it follows a sequence of Si particles primarily located on the cell boundaries (larger eutectic colonies are observed too) not too far from the main crack direction. As ΔK further increases, at $\Delta K >$ 11 to 12 MPa$\sqrt{\text{m}}$ (10 to 11 ksi$\sqrt{\text{in.}}$) Figure 7(a) (right), the crack follows almost exclusively the large Al-Si eutectic colonies. At this stage, the plastic zone is able to enclose a complete Al-Si eutectic Region or a succession of Al-Si eutectic Regions and thus a continuous network of damaged Al-Si eutectic islands becomes available to the incoming crack. This scenario roughly corresponds to the transition from Paris regime to Region III of faster propagation mode. The transitions are reflected in the changes of the fracture surface roughness. The Si particles can be regarded as brittle reinforcing particles in an *in-situ* composite material, and the boundaries between them and the matrix are Regions of high stress concentration favorable for crack propagation. At high ΔK levels, when the plastic zone is large and the cumulative strain damage is high, the number of fractured Si particles increases, even in the M structures, and cracks propagate *via* both debonding and fracture (Figures 7(b) and (c)).

It should be noted that the transition points in fatigue crack growth mechanisms are direct functions of the distances between consecutive available Si particle or whole Al-Si eutectic Regions (*i.e.*, Si particle distribution). The SDAS dictates the distribution as well as the size of the Al-Si eutectic Regions, and consequently it plays a critical role in the crack advance process. Large SDAS, besides resulting in higher long crack growth thresholds,[21] also induces

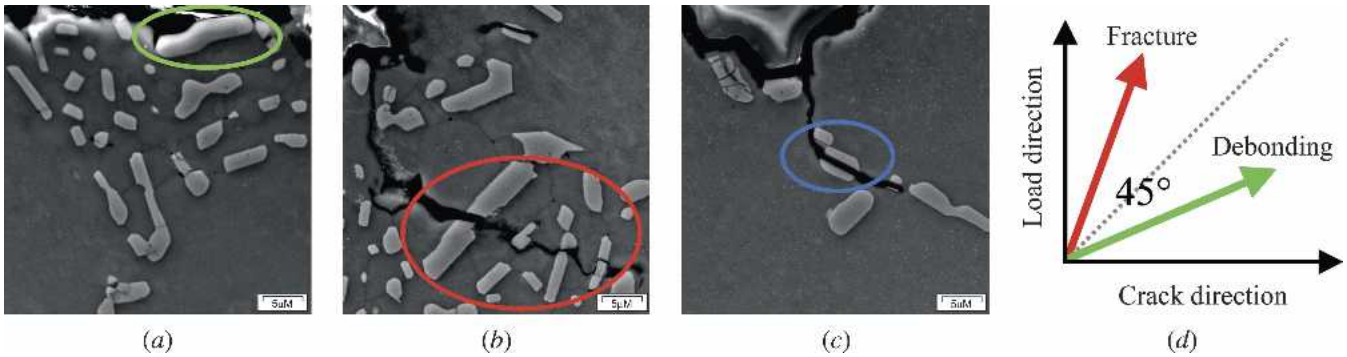

Fig. 6—Failure mechanisms for particles with high aspect ratio: (*a*) debonding, (*b*) fracture, and (*c*) fracture on twin plane; and (*d*) transition from debonding to fracture of high aspect ratio Si particles as a function of particle orientation with respect to load and crack directions.

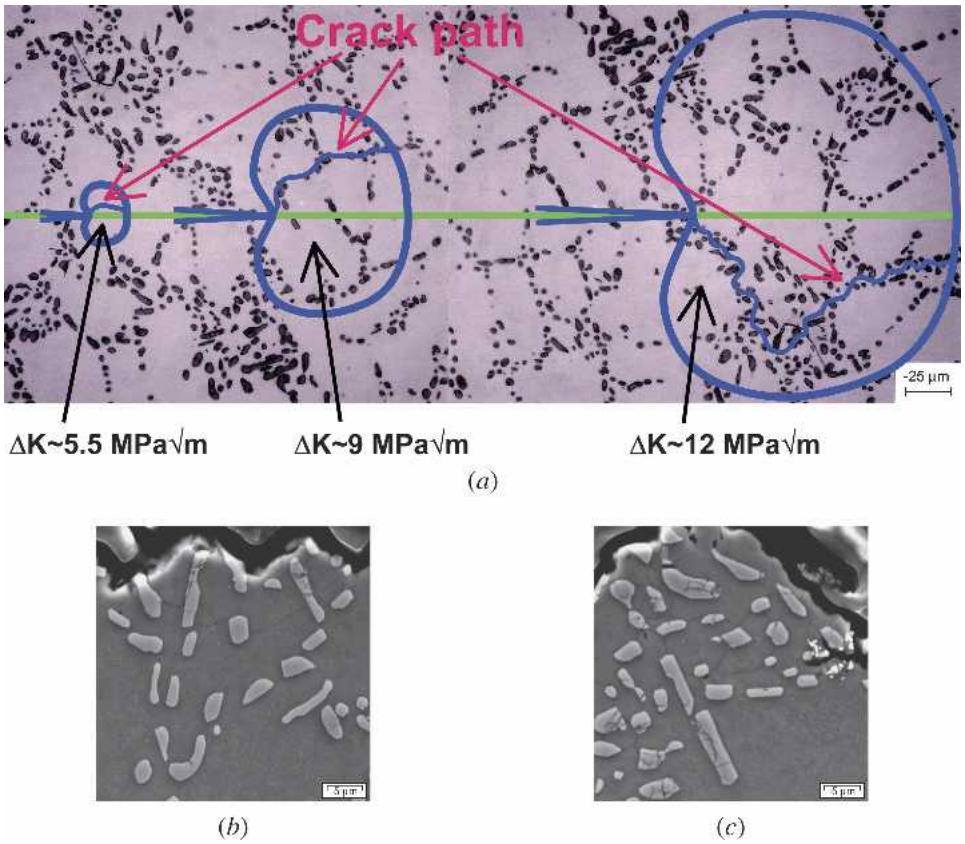

Fig. 7—(*a*) Plastic zone size representation at the microstructural scale of a 7 pct Si alloy for different ΔK levels; enlargements of the damaged Regions in the plastic zones at (*b*) $\Delta K \sim 9$ MPa$\sqrt{\text{m}}$, and (*c*) $\Delta K \sim 12$ MPa$\sqrt{\text{m}}$.

higher ΔK transitions from a predominant α-Al planar propagation mode to a preferential Si particle growth. By increasing the SDAS, the size of the plastic zone needed to envelop the same amount of Si particles has to be larger, and thus the transition from α-Al to Si occurs at a higher ΔK. Once the critical plastic zone is reached and the crack starts preferentially selecting Si particles, the fact that larger SDAS samples are also associated with larger Al-Si eutectic regions and coarser Si particles leads to higher growth rates in upper Region II and Region III, and lower pseudo-fracture toughness. Based on the understanding of microstructure related fatigue crack growth mechanisms, predictions for two 7 pct Si samples with similar M Si morphology and different SDAS values were qualitatively developed (Figure 8(a)). In Figure 8(a), the postulated, qualitative crack growth behavior for samples with SDAS values of ~70 to 80 μm (Figure 8(c)) and ~150 to 170 μm (Figure 8(d)) is compared with the experimental data for samples with small SDAS ~20 to 30 μm (Figure 8(b)). Similar behavior was experimentally observed for A356 squeeze and sand mold castings,[14] A356 permanent mold and sand mold castings,[15] and W319 (AA 320) castings.[16]

As mentioned earlier, the other critical parameter controlling the rate and mode of crack advance is related to the Si particles themselves. Alloys with higher Si content have more Si particles available at low crack driving forces,

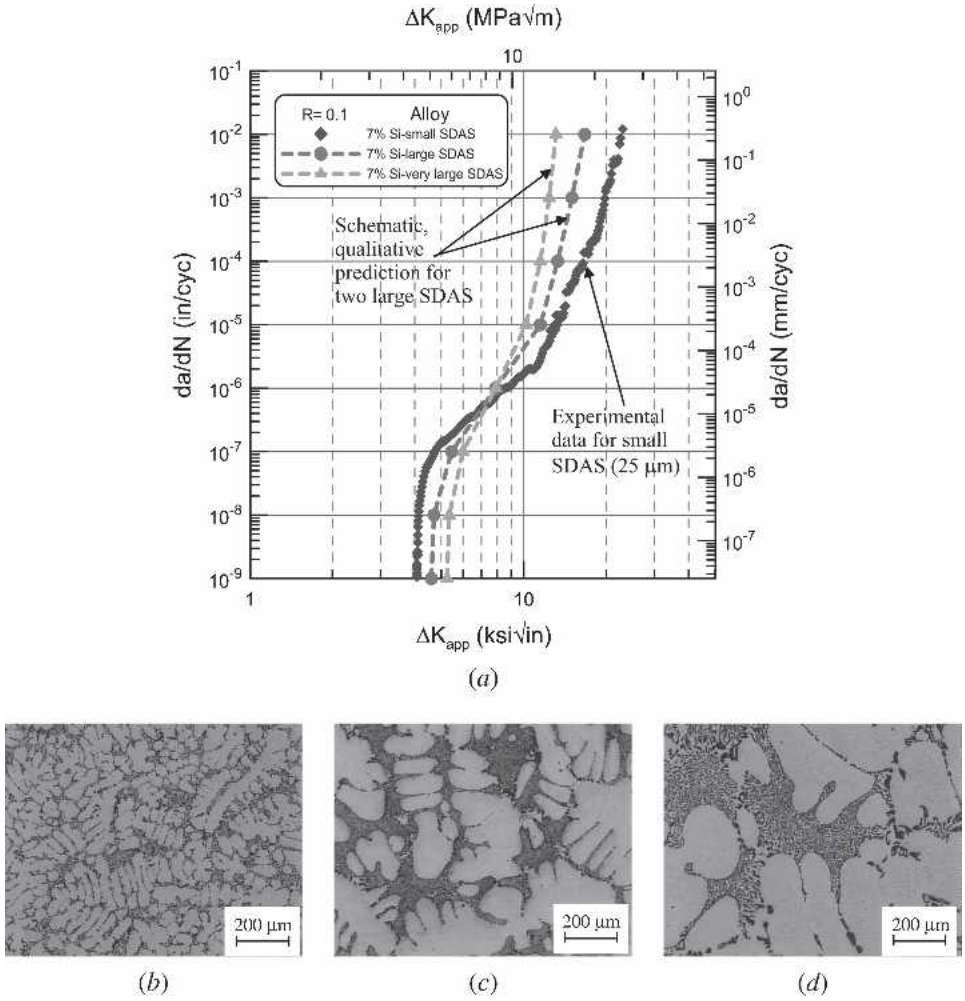

Fig. 8—(*a*) Postulated effect of SDAS on the fatigue crack growth behavior of a M 7 pct Si alloy for three SDAS levels; micrographs showing the microstructures of a 7 pct Si alloy with different SDAS: (*b*) small 20 to 30 μm; (*c*) large, 70 to 80 μm; and (*d*) very large, 150 to 170 μm.

faster crack advance at high ΔK levels, and lower pseudo-fracture toughness (Figures 2(a) and (b) and Figure 9).

Crack behavior in Region III is characterized by faster crack growth rates, with cracks exclusively following the eutectic Regions. The overload fracture in upper Region III occurs almost entirely through a ductile static tearing of the large Al-Si eutectic Regions. As a result, to a large extent, fracture toughness (the upper most ΔK value in Region III) is dictated by the Si particles' morphology (the ductile matrix fails through growth and coalescence of voids). Thus, the coarse/irregular Si morphology provides convenient paths for the crack to easily debond or cut through while the M Si morphology exerts more resistance to crack growth as the particles are more fracture resistant (Figure 9). The smaller, more defect free, and closer to the ideal spherical shape a reinforcing particle is, the higher its effective fracture strength is likely to be. Fracture strengths reported in the literature for pure single-crystal Si range from 7 GPa down to 300 MPa when a sharp stress concentrator is present.[27,28,29] Being spheroidized and small, M Si particles are less likely to experience such localized stress concentrations and are expected to exhibit a higher effective fracture stress. The irregularly shaped UM Si particles, on the other hand, are exposed to higher local stress concentrations compared to the rounder M Si particles, and therefore offer lower resistance to crack propagation due to a lower effective fracture strength (fracture strength reflecting the degree of irregularity of the Si particle as well as the presence of internal defects such as twins).

Similar to the fracture strength, there is a range of reported strengths in the literature for the debonding of the Al-Si interphase boundary.[30–33] These values are obtained from atomistic models, which assume given crystallographic planes to be in contact at the Al-Si interphase boundary. Some include the effects of vacancies, but no calculations have yet been made to include the effects of either line defects (such as dislocations intersecting the interphase boundary) or crystallographic defects within the Si phase itself (such as twins, commonly found in the Si phases of Al-Si alloys[34,35]). Moreover, they are generally calculated for an applied tensile force normal to the interphase boundary and include neither shear forces nor a configuration where the Al would be ''peeled'' away from the Si.

Under these assumptions, the reported values for the debonding strength range from 1.5 to over 20 GPa. In actual (not ideal) materials, values even lower than 1.5 GPa are likely to be found. Despite the overlap in the ranges

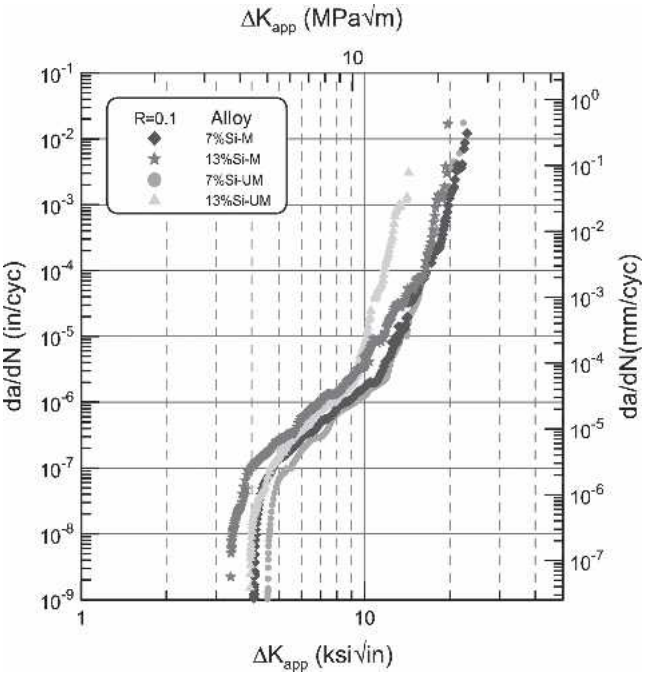

Fig. 9—Effects of Si morphology on the fatigue crack growth behavior of 7 pct Si and 13 pct Si alloys.

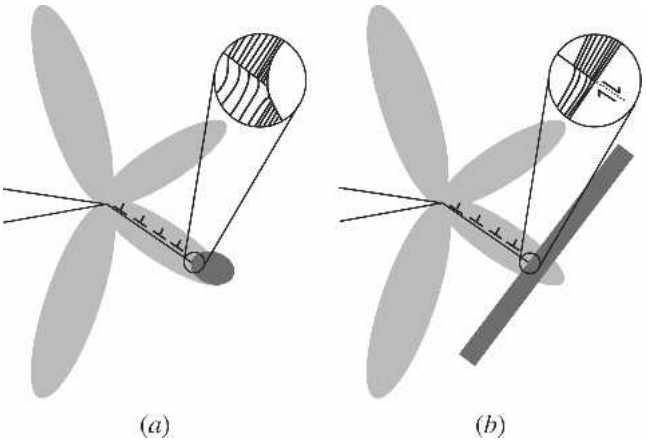

Fig. 10—Schematic representation of the effects of dislocation pile-ups on damage response of: (*a*) M, and (*b*) UM Si particles; the lobes represent shear stress zones around the crack tip.

reported for interfacial debonding and Si particle fracture strengths in imperfect engineering materials, when the role of Si morphology is taken into account, the observed damage mechanisms and changes in damage mechanisms can be rationalized. The small, rounded M Si morphology requires more energy for particle fracture (than debonding), and this is why a higher number of fractured particles are observed at increased ΔK. Specifically, when a dislocation pileup forming along a slip line reaches from the crack tip to an ''almost perfect, defect-free'' Si crystal, it creates an area of very high lattice strain at the interface boundary, which leads to the formation of a microcrack; since each dislocation represents an extra plane of atoms, an area of very high lattice strain forms at the interface boundary and the atomic plane deficient side of the slip line will essentially become an interphase microcrack (Figure 10(a)).

On the other hand, the irregular, coarse UM Si morphology does not require the same high energy for particle fracture and thus fractured particles can also be found at low ΔK (the UM particles are more sensitive to orientation with respect to the crack plane rather than the level of strain energy, as discussed earlier). Specifically, when a dislocation pileup forming along a slip line reaches from the crack tip to a ''large, less perfect'' Si crystal at a high angle, it creates a stress buildup against the Si particle, which will lead to fracture before interfacial damage can occur (Figure 10(b)). In this case, the strain energy is released through particle fracture likely aided by internal defects such as twins. It should be noted that M Si particles containing twins or at high strain energy can fracture, while UM Si particles with no twins near the surface can debond even when intersected by dislocations at a high angle.

The preceding explanations substantiate the response of M and UM alloys at high ΔK and also the relationship between Si morphology and fracture toughness. The M 7 pct Si alloys show slightly improved behavior in Region III compared to the UM ones, but the difference is less evident than in the case of 13 pct Si alloys. In the 7 pct Si alloys, the differences in Si morphology between UM and M alloys after heat treatment are not very large due to the thermal modification of the UM, platelike eutectic Si structure, which partly compensates for the chemical modification in the M alloys. On the other hand, compared to the UM 7 pct Si alloys, the larger plates in the UM 13 pct Si alloys do not undergo the same level of fragmentation and spheroidization during heat treatment. Thus, the degree of preservation of the platelike morphology dictates the differences between the UM and the M structures and drives the difference between the fatigue crack growth behavior in Region III of UM and M alloys. Larger differences in pseudo-fracture toughness are caused by larger differences in Si morphology, which is a function of Si content and heat treat time. The size and aspect ratio of Si particles for all the alloys are given in Table I, and the Si morphology ranking is in perfect agreement with the fracture toughness ranking of the Si containing alloys. Results of this study agree with the literature for A356 alloys[15,36] and Al-12 pct Si-0.35 pct Mg alloys[20] for tests conducted under constant stress ratio $R = 0.1$.

The monotonic material failure in upper Region III and final toughness values are strongly dependent on Si morphology and less on Si content. To predict toughness, model equations based on the size and the shape of the Si particles are needed: $\Delta K_{FT} = f$ (Si shape, Si size, Si distribution, and Si content). The importance of Si morphology rather than Si content can be clearly seen in Figures 2(a) and (b) for UM and M alloys, respectively. The M alloys with 7 and 13 pct Si have similar toughness due their comparable Si morphology, while the UM alloys show a toughness shift equivalent to the Si morphological differences.

The SEM analysis of the fracture surfaces for three alloys from 1 to 13 pct Si reveal the same characteristics explained earlier. In the hypoeutectic alloys, at low ΔK, fatigue striations corresponding to the crack advance through the Al matrix were observed on the fracture surfaces (the average striation spacing is comparable to the fatigue crack propagation rate at a given ΔK level) along with debonded or cracked Si particles or cavities from

which the Si particles had debonded. The eutectic alloys show no evidence of striations due to the absence of primary α-Al matrix (Figure 11). At high ΔK, characteristic dimples indicating ductile fracture in the matrix were found between Si particles.

Another important set of tests was performed on samples of the same composition subjected to various heat treatments (T61 and T4), Figure 12. Even though no significant differences were observed in the near-threshold regime (since closure mechanisms are mainly affected by the

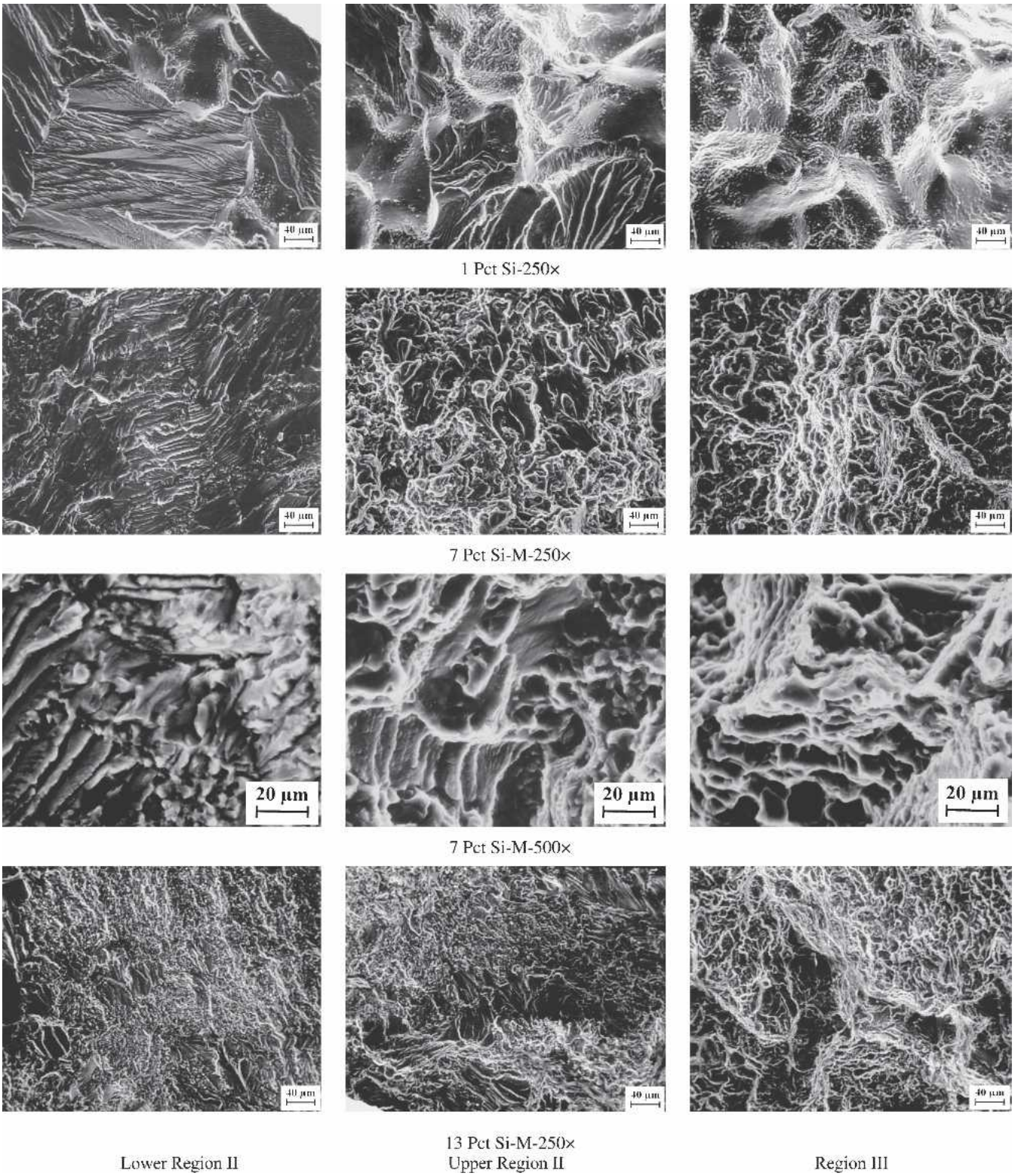

Fig. 11—Changes in fracture surface appearance with increasing ΔK (crack growth direction is from bottom to top).

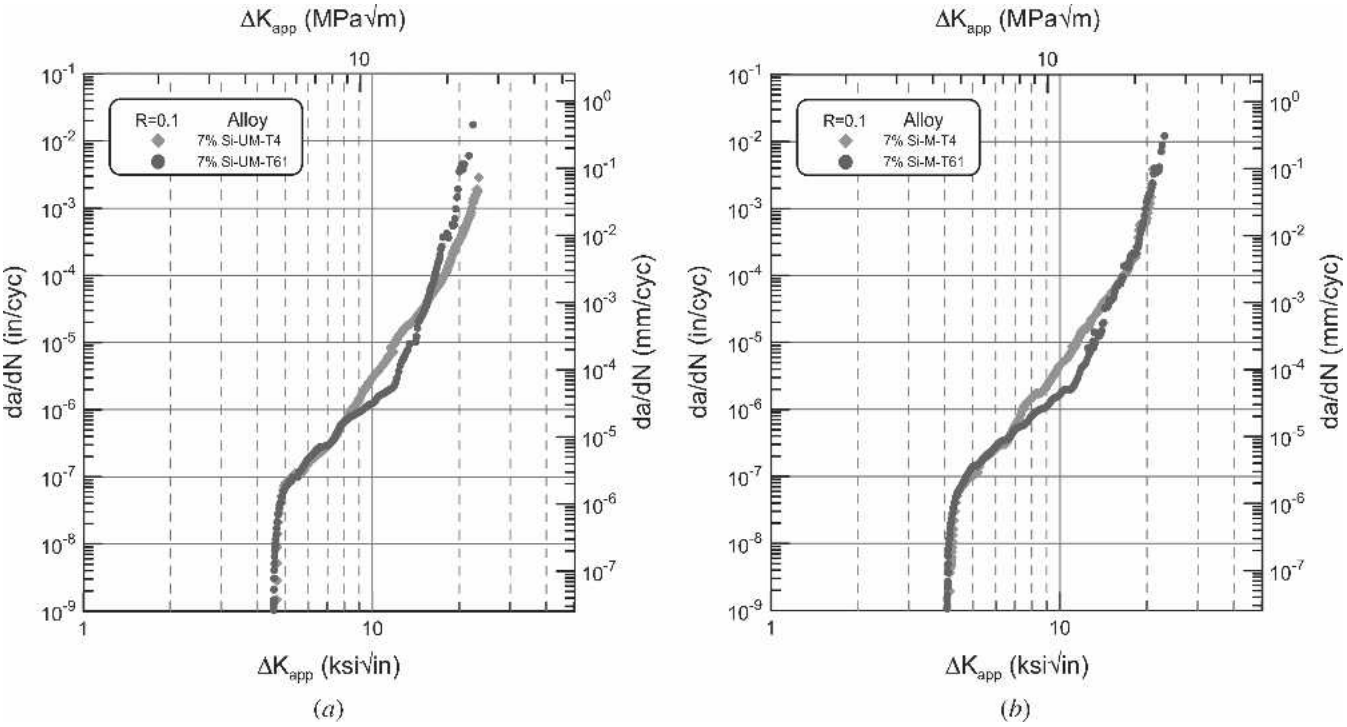

Fig. 12—Fatigue crack growth behavior of (*a*) UM, and (*b*) M 7 pct Si alloys in T61 and T4 heat treat conditions.

distribution and morphology of Si particles and not by the matrix strength[21]), differences were observed in mid and high Region II and Region III. In Region II, both the UM and M 7 pct Si alloys in T61 showed better fatigue crack growth resistance, while in Region III, the T4 samples lead to higher fracture toughness.

The differences in crack growth behavior of the T4 and T61 samples can be explained by associating the tendency of the crack to grow straight on a direction perpendicular to the applied load direction to the path of least resistance provided by the two microstructures (Figure 13).

In the absence of Mg-Si strengthening precipitates, the matrix of T4 samples is characterized by a lower yield strength compared to that of T61 tempered samples. Therefore, for the same stress intensities, larger plastic zones are reached in the T4 samples. Despite the larger plastic zones in the T4 samples, the weaker matrix may reduce the ability of the plastic zone to damage the eutectic structure (Al-Si interfaces or Si particles). Under these circumstances, the weaker α-Al matrix in T4 becomes another path of low resistance in front of the incoming crack (path 1 in Figure 13) in addition to the damaged Si particles/matrix interfaces or Si particles (path 2 in Figure 13); this occurs because the differences in crack resistance of the two structures are less significant than in T61 condition. The higher propagation rates in T4 samples are attributed to the weaker α-Al matrix, which facilitates crack growth and also promotes alternative local paths of low resistance for the crack to follow. Thus, fast growth can be achieved by local meandering along either path of low resistance located in the vicinity of the crack front instead of large scale meandering, following mainly the weak Si Regions away from the crack front, as observed in the T61 samples (high ΔK for T61 and T4 in Figure 13). The latter explains the reason why, at the same ΔK, a flatter fracture surface is observed in T4 samples compared to T61 samples. In addition, changes in damage accumulation mechanisms in the matrix phase can possibly be also associated with the naturally aged samples due to the loss of coherent precipitates. In upper Region III, T4 samples show a better fatigue crack growth resistance and higher pseudo-fracture toughness due to the ductile tearing of the softer Al matrix. Plastic flow at the crack tip blunts the crack and decreases the local stress. The crack growing by ductile tearing consumes a significant amount of energy by plastic flow, and the bigger the plastic zone (T4), the more energy is absorbed. Higher energy absorption leads to higher ΔK and ultimately higher fracture toughness, ΔK_{IC}. The differences in upper Region III are more evident when the linear elastic fracture mechanics definitions are corrected for plasticity and tearing contributions.[25] Similar observations in the threshold and upper Region III Regions were given in the literature for underaged and peak-aged samples of A356 alloys.[5,15]

The mechanisms presented in this study were reinforced by another set of experiments on UM and M 7 pct Si alloys with various grain size levels in the range 180 to 520 μm. Contrary to wrought alloys, where grain size plays an important role in fatigue crack growth and failure mechanisms,[37,38,39] cast alloys show low sensitivity to changes in grain size (Figure 14).

This behavior can be rationalized by taking into account the fact that cast alloys contain microstructural features smaller than grain size, such as eutectic Si particles and SDAS, which control the advance of the crack and dictate the levels where changes in mechanisms occur (Figure 15).

The extent of the plastic zone ahead of the crack tip affects these ''small-scale'' microstructural constituents as well as the interfaces between them first, before any grain

boundary is reached. Under these circumstances, the presence of grain boundaries becomes of secondary importance for grain size ranges typical for cast Al-Si alloys, 100 to 1000 μm. The interaction of the crack with the Si particles and the strength of the Al matrix/Si particles interface are the critical factors determining the crack advance rate at different crack driving forces (Figure 15).

Electron backscatter diffraction (EBSD) techniques were also used to observe the grain structure at different ΔK levels (Figure 16). The main objective was to reveal any possible preference of the cracks for certain crystallographic planes, and also to analyze if the preferential propagation through Al-Si eutectic Regions at high ΔK (upper Region II and lower Region III) is related to grain boundaries. No preferred orientation of the Al grains along the crack path was observed. No effects of either grain or subgrain boundaries on the crack propagation through the eutectic Regions at high crack driving forces were found. The secondary crack in Figure 16 reveals sampled Si particles located inside the grains, along the dendrite cell boundaries.

B. *Crack Propagation Mechanisms in Paris Region II and Region III for 1 Pct Si Alloys*

In the 1 pct Si alloys, with no/low eutectic Si, grain size has an effect on both the near-threshold regime due to differences in roughness-induced closure[21] and Regions II and III of crack growth. In Regions II and III, the observed changes in crack growth mechanisms from transgranular to intergranular (Figure 4 (top)) are again associated with the extent of the plastic zone ahead of the crack tip; the larger the stress intensity, the larger the plastic zone size and the greater the amount of grain boundary areas falling within it. Progressing from lower Region II to upper Region III, the plastic zone grows until it becomes sufficiently large to facilitate crack propagation exclusively along grain boundaries (Figure 17). For this category of alloys, grain size becomes the parameter controlling the fatigue crack growth mechanisms similar to wrought alloys. Thus, the distance between grain boundaries and the amount/area of grain boundaries play an important role in the fatigue crack growth response of these alloys (Figure 17).

It should be noted that for all alloys, the transition points, corresponding to either the Al-Si transition for 7 pct Si alloys or the transgranular-intergranular transition for 1 pct Si alloys (Figures 7(a) and 17), can also be reported in terms of critical K_{max} values, where $K_{max} = \Delta K/(1 - R)$. These critical values should be exceeded for the transitions to occur. For reverse engineering purposes, transition K_{max} values can also be estimated *a priori* using the plastic zone size required for a given transition to occur (which is a function of either SDAS or grain size) and the yield strength of the material. Thus, material/process evaluations can be performed before conducting experimental tests or in the absence of experimental data.

IV. CONCLUSIONS

As closure effects become less significant, fatigue crack growth mechanisms become strongly dependent on the matrix strength, the interface strength between primary α-Al structure and eutectic Si particles, and the effective

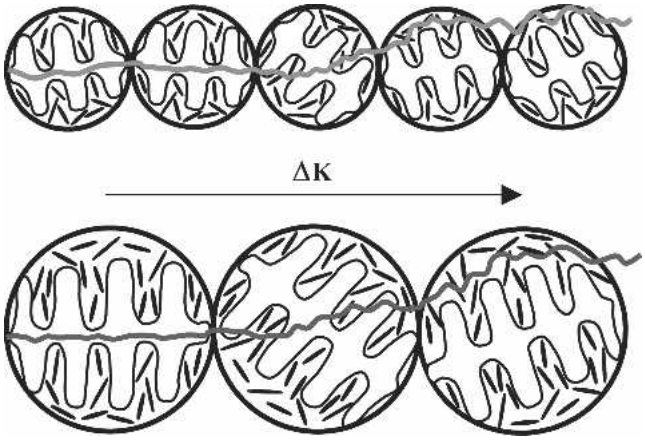

Fig. 15—Microstructural feature smaller than grain size govern fatigue crack growth behavior of 7 pct Si alloys.

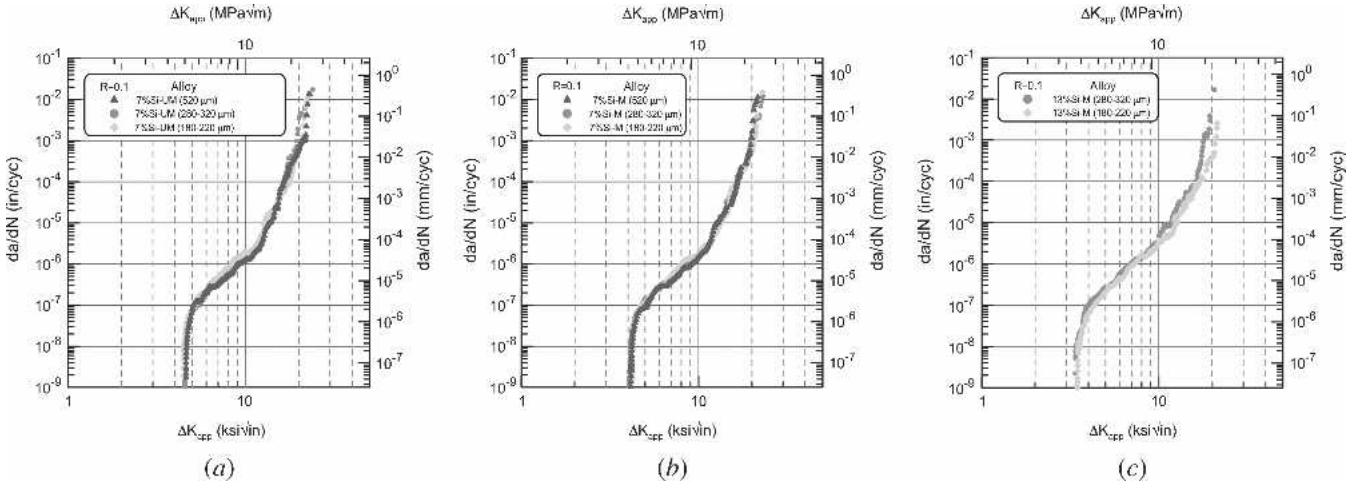

Fig. 14—Grain size effects on the fatigue crack growth behavior of (*a*) UM 7 pct Si alloys, (*b*) M 7 pct Si alloys, and (*c*) M 13 pct Si alloys.

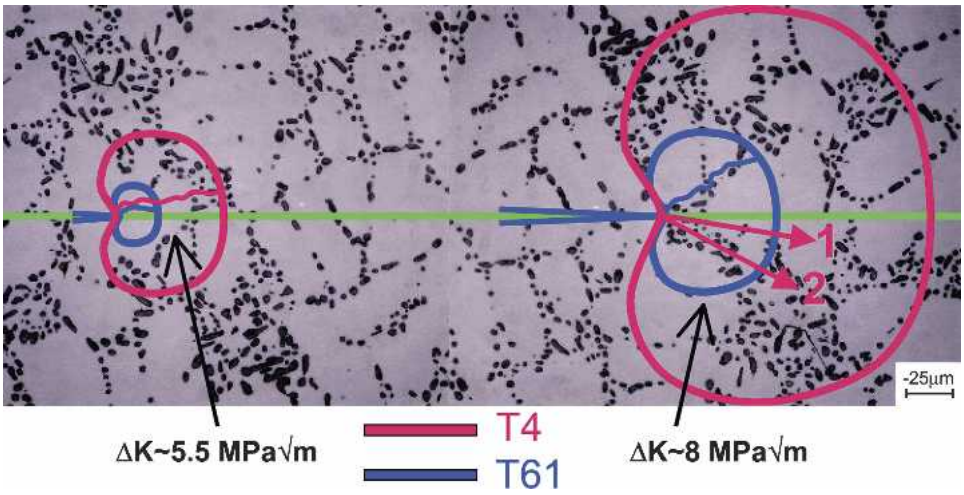

Fig. 13—Comparative changes in crack growth mechanisms with increasing ΔK for 7 pct Si alloys in T61 and T4 heat treat conditions.

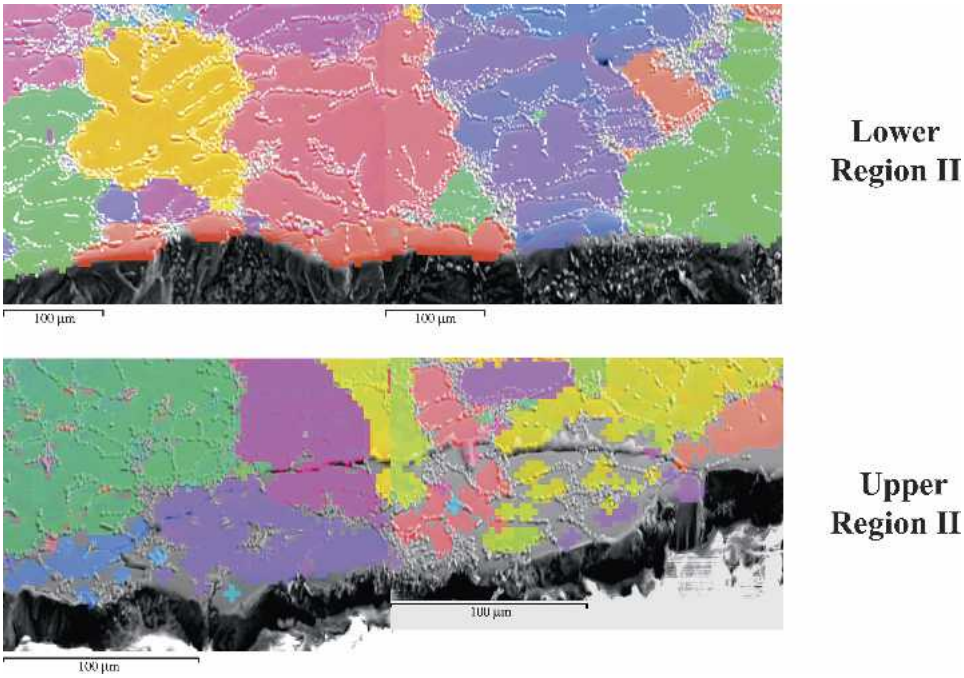

Fig. 16—Grain structure along the crack path of a M 7 pct Si alloy at two ΔK levels.

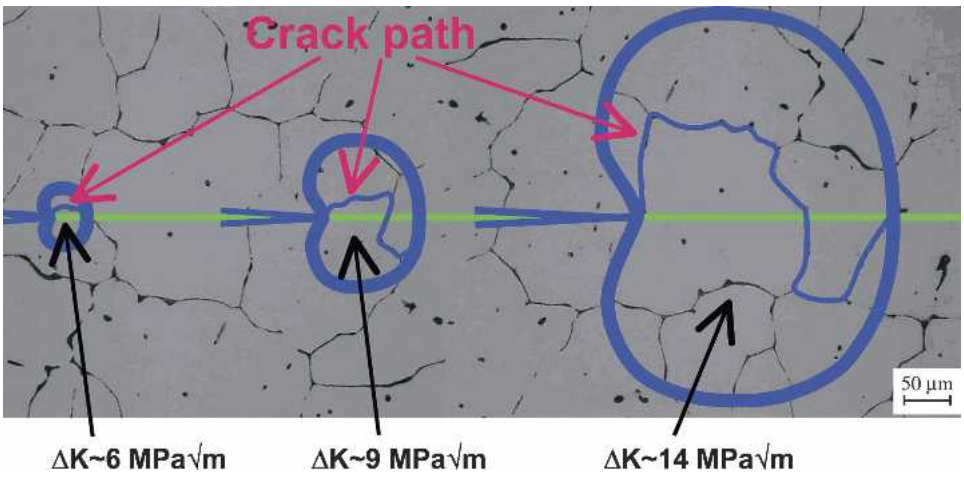

Fig. 17—Crack evolution with increasing ΔK for cast alloys with no/low eutectic phases (transgranular left and intergranular right).

Si particles strength. With increasing ΔK from lower Region II to upper Region II and Region III, the fracture surface roughness increases. This increase is associated with a change in fatigue crack growth mechanisms. While a flat surface corresponds to a crack propagating along the Al dendritic structure, a rough surface is a reflection of a preferential growth through the Al-Si eutectic Regions.

As a general rule, a crack always seeks the path of least resistance that is represented by the most damaged microstructural features ahead of it. Therefore, these changes in mechanisms were explained using correlations of the plastic zone size at various ΔK levels with the microstructural features enveloped by it. Small plastic zones restrict the availability of damaged Si particles (or interfaces with the Al matrix) and therefore restrain the possibility of crack meandering. This corresponds to a flat appearance of the crack with sporadic Si encounters. At high ΔK, however, the larger plastic zone size permits crack meandering through damaged Si particles away from the crack front, and this explains the preferential growth through the eutectic Regions.

In Region III, the crack advances preferentially through the Al-Si eutectic Regions, and very high crack growth rates in upper Region III are governed by ductile monotonic tearing. The alloys' behavior in this Region correlates well with Si morphology, and a fracture toughness ranking based on Si morphology was observed. Modified and low Si content alloys showed higher fracture toughness.

Differences between the behavior of T4 and T61 samples were observed away from the closure-affected Regions. While T61 shows a better fatigue crack growth resistance in upper Region II, T4 leads to higher toughness. The behavior of the T4 samples in Region II is explained by considering alternative paths of low resistance available. In Region III, the increased plasticity levels at the crack tip result in more blunted cracks, increasing the crack growth resistance and fracture toughness.

In the grain size range investigated, grain size plays a minimal role in the fatigue crack growth response of the studied alloys, due to the fact that fatigue crack growth advance is controlled by microstructural features smaller than the grain size (Si particles and SDAS). In the alloys with no eutectic Si (1 pct Si), grain size shows an effect similar to the one observed in wrought alloys.

REFERENCES

1. M.J. Couper, A.E. Neeson, and J.R. Griffiths: *Fatigue Fract. Eng. Mater. Struct.*, 1990, vol. 13 (3), pp. 213-27.
2. Q.G. Wang, D. Apelian, and D.A. Lados: *J. Light Met.*, 2001, vol. 1 (1), pp. 73-84.
3. H. Jiang, P. Bowen, and J.F. Knott: *J. Mater. Sci.*, 1999, vol. 34, pp. 719-25.
4. B. Skallerud, T. Iveland, and G. Harkegard: *Eng. Fract. Mech.*, 1993, vol. 44 (6), pp. 857-74.
5. J.A. Odegard and K. Pedersen: *SAE Technical Publication No. 940811*, SAE, Warrendale, PA, 1994, pp. 25-32.
6. J.C. Ting and F.V. Lawrence, Jr.: *Fatigue Fract. Eng. Mater. Struct.*, 1993, vol. 16 (6), pp. 631-47.
7. A. Wickberg, G. Gustafsson, and L.E. Larsson: *SAE Technical Publication No. 840121*, SAE, Warrendale, PA, 1984.
8. C. Nyahumwa, N.R. Green, and J. Campbell: *AFS Trans.*, 1998, vol. 106, pp. 215-23.
9. K. Shiozawa, Y. Tohda, and S.-M. Sun: *Fatigue Fract. Eng. Mater. Struct.*, 1997, vol. 20 (2), pp. 237-47.
10. B. Zhang, W. Chen, and D.R. Poirier: *Fatigue Fract. Eng. Mater. Struct.*, 2000, vol. 23, pp. 417-23.
11. S. Gungor and L. Edwards: *Fatigue Fract. Eng. Mater. Struct.*, 1993, vol. 16 (4), pp. 391-403.
12. D.A. Lados, D. Apelian, and A.M. de Figueredo: *Advances in Aluminum Casting Technology II*, Proc. Materials Solutions, M. Tiryakioglu and J. Campbell, eds., ASM, Metals Park, OH, 2002, pp. 185-96.
13. Q.G. Wang, D. Apelian, and D.A. Lados: *J. Light Met.*, 2001, vol. 1 (1), pp. 85-97.
14. S. Kumai, J. Hu, Y. Higo, and S. Nunomura: *J. Jpn. Inst. Light Met.*, 1995, vol. 45 (4), pp. 198-203 (in Japanese).
15. S. Kumai, S. Aoki, S.-W. Han, and A. Sato: *Mater. Trans., JIM*, 1999, vol. 40 (7), pp. 685-91.
16. M.J. Caton, J.W. Jones, J.M. Boileau, and J.E. Allison: *Metall. Mater. Trans. A*, 1999, vol. 30A, pp. 3055-68.
17. D.A. Lados and D. Apelian: *Mater. Sci. Eng., A*, 2004, vol. A385, pp. 200-11.
18. K.S. Chan, P. Jones, and Q. Wang: *Mater. Sci. Eng., A*, 2003, vol. A341, pp. 18-34.
19. K. Gall, N. Yang, M. Horstemeyer, D.L. McDowell, and J. Fan: *Metall. Mater. Trans. A*, 1999, vol. 30A, pp. 3079-88.
20. F.T. Lee, J.F. Major, and F.H. Samuel: *AFS Trans.*, 1996, vol. 104, pp. 785-95.
21. D.A. Lados, D. Apelian, and J.K. Donald: *Acta Mater.*, 2006, vol. 54 (6), pp. 1475-86.
22. D.A. Lados, D. Apelian, P.C. Paris, and J.K. Donald: *Int. J. Fatigue*, 2005, vol. 27 (10–12), pp. 1463-72.
23. J.K. Shang, W. Yu, and R.O. Ritchie: *Mater. Sci. Eng., A*, 1988, vol. A102, pp. 181-92.
24. Y. Sugimura and S. Suresh: *Metall. Mater. Trans. A*, 1992, vol. 23A, pp. 2231-42.
25. D.A. Lados and D. Apelian: *Eng. Fract. Mech.*, 2006, vol. 73 (4), pp. 435-55.
26. R.C. McClung and H. Sehitoglu: *Eng. Fract. Mech.*, 1989, vol. 33, pp. 237-71.
27. K.E. Petersen: *Proc. IEEE*, 1982, vol. 70 (5), pp. 420-57.
28. B. Stark: in *MEMS Reliability Assurance Guidelines for Space Applications*, ch. 4, *Material Properties*, JPL Publication 99-1, NASA, Pasadena, CA, 1999, pp. 49-68.
29. S.M. Spiering: *Acta Mater.*, 2000, vol. 48, pp. 179-96.
30. M. Horstemeyer: *Microstructure Property Modeling in Design and Product Optimization for Cast Light Metals*, USAMP-LMD 110 Project, AFS, Des Plaines, IL, 2001.
31. K. Gall, M.F. Horstemeyer, M. Van Schilfgaarde, and M.I. Baskes: *J. Mech. Phys. Solids*, 2000, vol. 48, pp. 2183-212.
32. D.K. Ward, W.A. Curtin, and Y. Qi: *Aluminum-Silicon Interfaces and Nanocomposites: A Molecular Dynamics Study—Research on "Interfaces and Coatings,"* General Motors–Brown University Collaborative Research Laboratory, Brown University, Providence, RI, 2004.
33. K.A. Peterson, I. Dutta, and M. Chen: *J. Mater. Proc. Technol.*, 2004, vol. 145, pp. 99-108.
34. S.Z.-Lu and A. Hellawell: *Metall. Mater. Trans. A*, 1987, vol. 18A, pp. 1721-33.
35. M. Shamsuzzoha and L.M. Hogan: *J. Cryst. Growth*, 1986, vol. 76, pp. 429-39.
36. M.D. Dighe and A.M. Gokhale: *Scripta Metall.*, 1997, vol. 37, pp. 1435-40.
37. J.A. Odegard: Ph.D. Thesis, Norwegian Institute of Technology, Trondheim, Norway, 1992.
38. A. Turnbull and E.R. de los Rios: *Fatigue Fract. Eng. Mater. Struct.*, 1995, vol. 18 (11), pp. 1355-66.
39. G.A. Osinkolu, G. Onofrio, and M. Marchionni: *Mater. Sci. Eng., A*, 2003, vol. A356, pp. 425-33.